New Journal of Physics
The open access journal at the forefront of physics

Deutsche Physikalische Gesellschaft DPG
IOP Institute of Physics

Published in partnership with: Deutsche Physikalische Gesellschaft and the Institute of Physics

OPEN ACCESS

RECEIVED
19 July 2021

REVISED
28 September 2021

ACCEPTED FOR PUBLICATION
15 October 2021

PUBLISHED
2 November 2021

PAPER

A single-laser scheme for observation of linear Breit–Wheeler electron–positron pair creation

Y He[1], I-L Yeh[2], T G Blackburn[3] and A Arefiev[1,*]

[1] Department of Mechanical and Aerospace Engineering, University of California at San Diego, La Jolla, CA 92093, United States of America
[2] Department of Physics, University of California at San Diego, La Jolla, CA 92093, United States of America
[3] Department of Physics, University of Gothenburg, SE-41296 Gothenburg, Sweden
[*] Author to whom any correspondence should be addressed.

E-mail: aarefiev@eng.ucsd.edu

Keywords: linear Breit–Wheeler process, high-intensity laser, laser–plasma interaction, particle-in-cell simulation

Abstract

We show that a single laser pulse, traveling through a dense plasma, produces a population of MeV photons of sufficient density to generate a large number of electron–positron pairs via the linear Breit–Wheeler process. While it may be expected that the photons are emitted predominantly in the forward direction, parallel to the laser propagation, we find that a longitudinal plasma electric field drives the emission of photons in the backwards direction. This enables the collision of oppositely directed, MeV-level photons necessary to overcome the mass threshold for the linear Breit–Wheeler process. Our calculations predict the production of 10^7 electron–positron pairs, per shot, by a laser with peak intensity of just 3×10^{22} W cm^{-2}. By using only a single laser pulse, the scheme sidesteps the practical difficulties associated with the multiple-laser schemes previously investigated.

1. Introduction

With the development of modern laser technology, the intensity of state-of-the-art lasers has surpassed the level of 10^{22} W cm^{-2} [1–3]. Under electromagnetic fields of such magnitude, which are able to accelerate particles to ultrarelativistic energies, effects of quantum electrodynamics (QED) are expected to become important [4]. This capability has led to wide interest in using ultra-intense lasers to study strong-field QED phenomena, the theory of which has been developed for at least sixty years [5–7]. Experimental investigation of the strong-field regime is at an early stage [8, 9], but is expected to develop significantly as the next generation of high-intensity laser facilities are commissioned.

It is of particular interest to investigate the annihilation of two photons into an electron–positron pair, or the linear Breit–Wheeler process ($\gamma + \gamma \rightarrow e^- + e^+$) [10], using the most advanced laser facilities. The linear Breit–Wheeler process, besides being a fundamental prediction of the theory of QED, also has important applications in astrophysics: for example, in understanding the opacity of the Universe [11] and in studying the pair cascade in pulsar magnetospheres [12–15]. Despite its importance, however, it has never been observed in a laboratory with real photons. The experimental difficulty comes from its small cross section and its MeV center-of-mass energy threshold. To overcome these difficulties, a system with colliding dense multi-MeV photons is required. Various geometries have been proposed, including the combination of GeV bremsstrahlung photons with keV blackbody photons produced in a hohlraum [16] or with an intense x-ray laser pulse [17]; the combination of multi-MeV photon beams each produced by a separate laser-irradiated foil or low-density plasma targets [18–22]; and the combination of multi-MeV photon beams produced by two colliding laser pulses within a structured target [23].

However, in these works, multiple laser pulses are required in one experiment, which limits the choice of facility where the proposed experiments can be conducted. Moreover, if the photon beams are generated in separate sources, then they must travel over a certain distance to reach the collision point. This leads to two

limiting factors for the possible pair yield. First, alignment and overlap of the photon beams is not automatically achieved. Second, during the propagation of beams, the divergence reduces the photon density, which scales as $1/R^2$, where R is the distance between the photon source and the collision region. The number of binary photon collisions scales as the product of photon densities, i.e. as $1/R^4$, and therefore the yield of electron–positron pairs is suppressed.

In this paper, we show that, during the propagation of a *single* laser pulse along a plasma channel, more than 10^7 pairs can be produced by the linear Breit–Wheeler process inside the plasma target, where currently available 10^{22} W cm^{-2} class laser pulses and targets [24] are used. The key feature which explains this high yield is an unexpected emission of MeV photons in the opposite (backward) direction to the laser propagation: indeed, our simulations show that the numbers of photons emitted backwards and forwards, in the keV to MeV energy range, are of the same order of magnitude. This is unexpected because electrons, under the action of the laser fields and the azimuthal magnetic field generated by their collective motion, are expected to be accelerated parallel to the direction of laser propagation [25–27], and therefore to emit photons overwhelmingly forward. The backward moving photons collide with these forward moving photons, usually focused on in studies of direct laser acceleration (DLA) [28], and produce linear Breit–Wheeler pairs. Since both the backward and forward moving photons are created inside the same plasma channel, photon density remains high at the time of collision.

This paper examines and explains the origin of the backward-moving MeV photons. We find that, as the laser propagates along the plasma channel, a longitudinal electric field is induced at the leading edge of the laser pulse due to charge separation. The longitudinal field co-propagates with the laser pulse, accelerating some of the channel electrons backwards after they encounter the laser pulse. The interaction of the backward-moving electrons with the propagating laser pulse causes them to emit energetic MeV-level photons. The emission process is enhanced due to the counter-propagating geometry of the interaction. These are the photons that cause the observed two-photon pair production inside the channel when they collide with the forward-emitted gamma-rays.

The rest of this paper is organized as follows. In section 2, we review the key elements of a laser–plasma interaction where a high-intensity laser pulse propagates through a relativistically-transparent target and the generation of a collimated beam of energetic gamma-rays associated with it. In section 3, we examine the source of backward-directed gamma-rays that are also present, but frequently overlooked, in the considered interaction. In section 4, we show that binary collisions between the forward and backward-directed photons of the right energy range occur frequently enough to generate an appreciable yield of electron–positron pairs. In section 5, we develop a reduced test-particle model and then apply it to examine the backward electron acceleration that leads to the emission of the backward-directed gamma-rays and assess the impact of the plasma electric and magnetic fields on the electron dynamics. In section 6, we summarize our findings.

2. Emission of forward-directed collimated gamma-rays

It is now well-recognized that a high-intensity laser pulse propagating through a relativistically-transparent plasma can efficiently generate a collimated beam of energetic gamma-rays [22, 24, 28–31]. In this section, we review the main physics elements of this process. A comprehensive analysis is available in [22, 32].

The emission of collimated energetic gamma-rays is closely associated with the presence of a strong quasi-static azimuthal magnetic field inside the laser-irradiated plasma. The field is generated and maintained by a volumetrically distributed longitudinal electron current driven by the propagating laser pulse. Figure 1 illustrates this phenomenon for a 25 fs, 800 nm laser beam with a peak intensity of $I_0 \sim 3 \times 10^{22}$ W cm^{-2} propagating through a structured plastic target with a pre-filled channel. The beam has the parameters similar to those expected at the ELI-NP laser facility [1]. Detailed laser and target parameters and the information regarding the simulation setup are given in the appendix. Figure 1(a) shows stable propagation of the laser beam through the channel and figure 1(c) shows a time-averaged magnetic field (the averaging is performed over one laser period) generated as a result of this propagation.

The magnitude of the quasi-static magnetic field in the considered example is very high—it is 3 GG or 20% of the strength of the oscillating laser magnetic field (in the absence of the target). Such a strength is achieved by using a channel with an electron density that is higher than the classical cutoff density $n_c = \pi mc^2/(e\lambda_0)^2$ for a laser with a vacuum wavelength of $\lambda_0 = 800$ nm, where c is the speed of light and e and m are the electron charge and mass. In our example, the normalized laser amplitude, defined as $a_0 = 0.85 I_0^{1/2}[10^{18}\ \text{W cm}^{-2}]\lambda_0[\mu\text{m}]$, is $a_0 = 120$. The fact that $a_0 \gg 1$ means that the electrons in the irradiated plasma become relativistic. This, in turn, raises the cutoff density to approximately $a_0 n_c = 120 n_c$, making the plasma in the channel, whose density is $n_e \approx 2.8 n_c$, transparent. The increased plasma

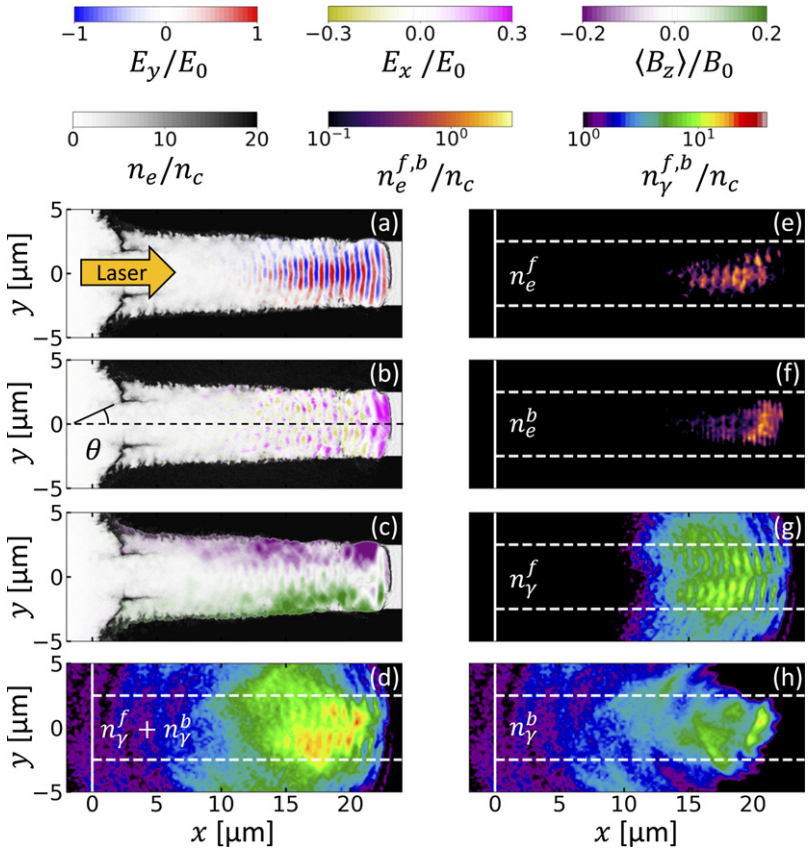

Figure 1. Propagation of a laser pulse with $a_0 = 120$ inside a structured target and the resulting generation of gamma-rays. (a) and (b) Transverse, E_y, and longitudinal, E_x, electric fields normalized to $E_0 = 1.61 \times 10^{10}$ statV/cm. (c) Time-averaged (over one laser period) magnetic field, $\langle B_z\rangle$, normalized to $B_0 = 16.1$ GG. (d) The density of emitted photons with energy greater than 100 keV. (e) Density of forward moving electrons with $\chi_e > 0.03$ and $\gamma_e > 15$. (f) Density of backward moving electrons also with $\chi_e > 0.03$ and $\gamma_e > 15$. The characteristic photon energy, $\overline{\varepsilon}_\gamma$, of the photons emitted by the electrons selected in (e) and (f) is greater than 100 keV. (g) Density of forward moving photons with energy greater than 100 keV. (h) Density of backward moving photons with energy greater than 100 keV. Electron and photon densities are normalized to the critical density n_c. All of the snapshots are taken at $t = 67$ fs.

transparency is a manifestation of a more general phenomenon referred to as *relativistically induced transparency* [33–36]. The channel is used in our simulation to stabilize the laser propagation [28, 37], with the dense walls ($n_e \approx 28n_c$) providing optical guiding. The mechanism described here and the resulting electron acceleration and photon emission discussed in this section have been shown not to be sensitive to the bulk density. For example, similar simulations have been performed in [22] with a bulk electron density of $100n_c$. Structured targets with foam-filled channels have been successfully fabricated by general atomics and used for an experimental campaign at the Texas Petawatt laser facility [24].

The plasma magnetic field has two important functions: to enhance laser-driven electron acceleration and to induce emission of energetic photons by the accelerated electrons. At $a_0 \gg 1$, DLA produces forward moving electrons due to a forward push by the Lorentz force of the laser magnetic field. Transverse deflections by the plasma magnetic field can keep the transverse electron velocity anti-parallel to the transverse laser electric field and thus enable the accelerated electrons to continue gaining energy despite the oscillations of the laser electric field [32]. The deflections are particularly effective when the frequency of transverse electron oscillations caused by the magnetic field is comparable to the Doppler shifted frequency of the laser [38, 39]. Such a condition can be realized only in a plasma with a sufficiently high current density [32]. In our simulation, the electrons reach a maximum energy of 700 MeV through the described mechanism. The deflections by the magnetic field not only enable the electrons to gain more energy from the laser field, but they also lead to energy losses via synchrotron emission of electromagnetic radiation. The rate of the energy gain typically greatly exceeds the rate of energy losses associated with the emission, so the laser accelerated electrons can efficiently convert the laser energy carried by optical photons into gamma-rays.

The photon emission process by an electron with a velocity $\boldsymbol{v}$ is characterized by a dimensionless parameter

$$\chi_e = \gamma_e \mathcal{E}/B_{crit}, \tag{1}$$

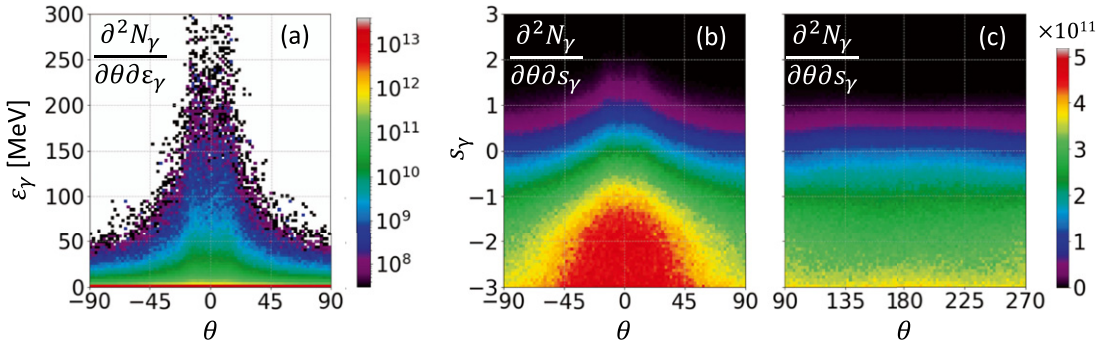

Figure 2. Energy-angle spectra of the photons emitted inside the structured target from figure 1. (a) and (b) The distribution of the forward-directed photons on linear and logarithmic energy scales, where $s_\gamma \equiv \log_{10}(\varepsilon_\gamma[\mathrm{MeV}])$. (c) The distribution of the backward-directed photons on a logarithmic energy scale. Here θ is the angle defined in figure 1(b).

with $\mathcal{E}$ being an effective transverse field strength:

$$\mathcal{E} = \sqrt{\left(\boldsymbol{E} + \frac{1}{c}[\boldsymbol{v}\times\boldsymbol{B}]\right)^2 - \frac{1}{c^2}(\boldsymbol{E}\cdot\boldsymbol{v})^2}. \tag{2}$$

Here $\boldsymbol{E}$ and $\boldsymbol{B}$ are the electric and magnetic fields acting on the electron, $\gamma_e = 1/\sqrt{1 - v^2/c^2}$ is the relativistic factor, and $B_{\mathrm{crit}} \approx 4.4 \times 10^{13}$ G is the magnetic equivalent of the well-known Schwinger (or critical) electric field [40]. The characteristic energy of emitted photons, $\overline{\varepsilon}_\gamma$, is given by [41]

$$\overline{\varepsilon}_\gamma = 0.44\gamma_e\chi_e mc^2, \tag{3}$$

These photons are emitted in the direction of the electron momentum into a narrow cone whose opening angle is roughly $1/\gamma_e$. As a result, forward moving electrons generate a forward-directed beam of photons.

In the case of ultra-relativistic forward-moving electrons, like those generated by the laser in the presence of the plasma magnetic field, the contributions from the laser electric and magnetic fields to the effective field $\mathcal{E}$ nearly cancel each other out. Therefore, one can estimate $\mathcal{E}$ by simply using the plasma magnetic field B^{pl}, with $\mathcal{E} \approx B^{\mathrm{pl}}$, which yields the following approximate expression for χ_e:

$$\chi_e \approx \gamma_e B^{\mathrm{pl}}/B_{\mathrm{crit}}. \tag{4}$$

It follows from this estimate that we have $\chi_e \approx 0.020$ for an electron with $\gamma_e \approx 300$ that is deflected by $B^{\mathrm{pl}} \approx 3$ GG $\approx 0.19B_0$, which is close to the maximum amplitude of the quasi-static field shown in figure 1(c). The characteristic photon energy is $\overline{\varepsilon}_\gamma \approx 1.4$ MeV. This example illustrates the important role played by the plasma magnetic field in generating energetic gamma-rays.

The spectrum of forward-emitted photons in our simulation is shown in figure 2(a). It is indeed well-collimated in the forward direction, in agreement with our expectations. The photon spectrum is broad because the synchrotron spectrum is itself broadband and because electrons with a wide range of energies contribute to the emission. In our simulation, the photon emission is modeled using a Monte Carlo module for quantum synchrotron radiation [42]. The module computes χ_e at each time-step for each charged macro-particle. This value is then used to determine the energy and number of emitted photons. The finite width of the emission cone is neglected, so the photons are emitted along the momentum of the emitting particle. The module also self-consistently accounts for the recoil experienced by the particle when emitting individual photons, as described in [42, 43].

3. Emission of backward-directed gamma-rays

In section 2, we reviewed how a high-intensity laser pulse propagating through a relativistically-transparent plasma can efficiently generate a collimated beam of energetic gamma-rays. In what follows, we discuss the source of backward-directed gamma-rays that are also present, but frequently overlooked, in the considered setup.

Figure 2(c) shows that indeed, in addition to forward-directed gamma-rays, the plasma electrons in our simulation emit energetic backward-directed photons. These photons, which have an almost uniform angular distribution, originate from electrons that are moving backwards over at least some segments of their trajectories. The backward-emitting electrons are concentrated primarily at the leading part of the

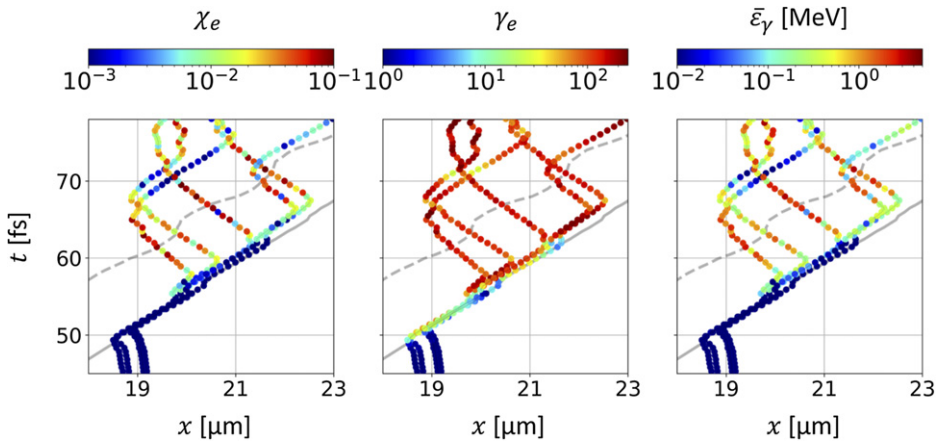

Figure 3. Time evolution of χ_e, γ_e, and $\bar{\varepsilon}_\gamma$ along trajectories of five randomly selected electrons from inside the channel. The solid and dashed gray curves indicate the extent of the localized E_x structure shown in figure 4(a) and located at the front of the propagating laser pulse. The curves show the locations where E_x is 10% of max(E_x) at each time instant.

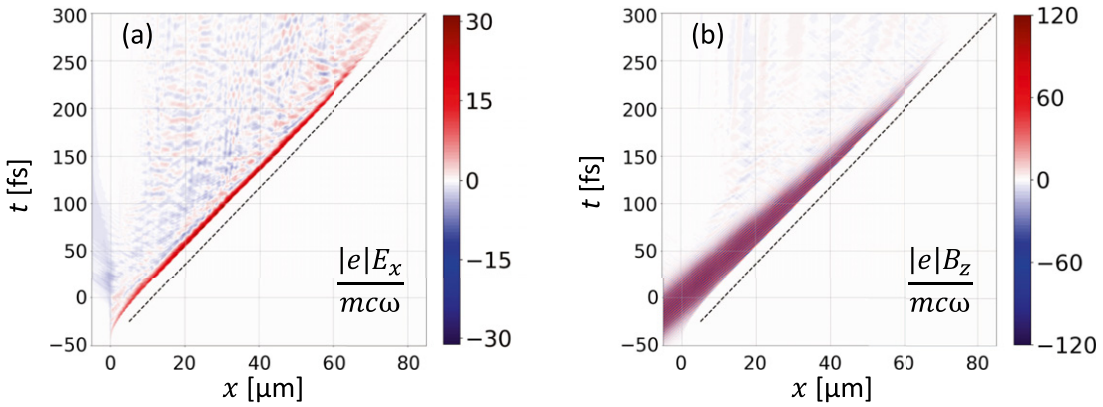

Figure 4. Temporal evolution of E_x and B_z in the near-axis region in the PIC simulation shown in figure 1. The fields are spatially averaged in the transverse direction over a region with $|y| < 1.5$ μm. The dashed black lines is the same in both panels, represent motion along x with velocity $v_x = 0.82c$.

laser pulse: this may be seen in figure 1(f), which shows the density of electrons that have $p_x < 0$, $\gamma_e > 15$ and $\chi_e > 0.03$. In order to identify their origin, we track five randomly selected electrons that are initially located inside the channel prior to the arrival of the laser pulse. The electrons were selected, at $t = 17$ fs, from the region defined by $|y| < 0.5$ μm and 18.75 μm $< x <$ 19.25 μm. As seen in figure 3, these electrons reverse the direction of their longitudinal motion after being swept up by the leading edge of the laser pulse.

The backward acceleration of the electrons inside the channel is caused by a longitudinal electric field, E_x, which is shown in figure 1(b) at $t = 67$ fs. This field is concentrated at the leading edge of the laser pulse. It is formed by charge separation as the laser enters the plasma channel, displacing electrons ahead of the much heavier and therefore slower moving ions, and moves forward with the leading edge of the laser pulse. This aspect is shown in figure 4, where figure 4(a) shows the time evolution of E_x in the region close to the axis and figure 4(b) shows the time evolution of the time-dependent magnetic field B_z, associated primarily with the laser, in the same region. At each location along x, both fields are a spatial average over the region $|y| < 1.5$ μm. We find that the E_x structure moves with a constant speed of $0.82c$ and that its amplitude is slowly varying after the initial ramp-up. The field structure disappears by about $x \approx 70$ μm following the laser depletion, which again confirms that it is driven by the laser pulse itself.

In contrast to the case of the forward-moving electrons, the effective field $\mathcal{E}$ for the backward-propagating electrons is primarily determined by the fields of the laser. The reason for this difference is the lack of compensation between $\boldsymbol{E}$ and $\boldsymbol{B}$ of the laser. These fields are much stronger than the fields created by the plasma, so, in the absence of their compensation, they dominate the expression for $\mathcal{E}$ given by equation (2). Therefore we neglect the plasma fields, set $\boldsymbol{E}^{\rm laser} = \boldsymbol{B}^{\rm laser}$, and assume that the electron is moving purely backwards to find that the effective field acting on the backward-moving electrons is $\mathcal{E} \approx 2B^{\rm laser}$. This effective field is stronger than the effective field for the forward moving electrons by a

factor of $2B^{\rm laser}/B^{\rm pl} \approx 13$ [in our case $\max(B^{\rm laser}) \approx 20$ GG]. Thus, while a relativistic factor of $\gamma_{\rm e} \approx 300$ would be necessary for a forward-moving electron to have a typical photon energy of 1.4 MeV, only $\gamma_{\rm e} \approx 80$ is necessary for a backward-moving electron to emit photons with the same energy.

4. Yield of electron–positron pairs via the linear Breit–Wheeler process

As discussed in sections 2 and 3, the laser–plasma interaction under consideration generates a gamma-ray population with both backward and forward moving photons. Figures 2(b) and (c) show that the energies of these photons exceed 100 keV and reach 10 MeV, even for the backward emission. This energy range is favorable for the electron–positron pair creation via binary photon collisions, i.e. the linear Breit–Wheeler process, because it can overcome the center-of-mass energy threshold:

$$\varepsilon_\gamma^{\rm f}\varepsilon_\gamma^{\rm b} > \left(mc^2\right)^2, \tag{5}$$

where $\varepsilon_\gamma^{\rm f}$ and $\varepsilon_\gamma^{\rm b}$ are the energies of the forward and backward-directed colliding photons. In this section, we show that, in the interaction, binary collisions between photons of the right energy range occur frequently enough to generate an appreciable yield of electron–positron pairs.

Photon collisions are possible only if the backward-moving photons are emitted ahead of forward-moving photons. As these photons are emitted by backward and forward-moving electrons, respectively, we examine the spatial distribution of these two components of the electron population, selecting only those electrons which have $\gamma_{\rm e} > 15$ and $\chi_{\rm e} > 0.03$. We apply this selection criterion because, according to equation (3), the characteristic energy of the photons emitted by such electrons is $\overline{\varepsilon}_\gamma > 100$ keV, which is within the favorable energy range for the linear Breit–Wheeler process. Snapshots of the density for backward and forward-moving electrons, selected according to the described criterion, are shown in figures 1(e) and (f), respectively. The forward-moving and thus forward-emitting electrons are spread throughout entire region occupied by the laser pulse (see figure 1(a)). The backward emitting electrons, by contrast, are primarily concentrated at the front of the laser pulse. This is in good agreement with the mechanism of their generation by E_x at the leading edge of the laser pulse (see figure 1(b)).

The difference in the spatial localization of the emitting electrons translates into photon emission profiles that are favorable for the photon–photon collisions. Figure 5(b) shows snapshots of $\partial^2 N_\gamma/\partial x\partial t$ for forward and backward-directed photons, where N_γ is the number of photons with energy between 100 keV and 10 MeV emitted in a thin vertical slice. We can see from the two curves that the backward-moving photons are emitted ahead of the forward-moving photons. For completeness, figure 6 shows the energy distribution of the forward and backward directed electrons in our simulation. The snapshots in figures 6 and 5 are taken at $t = 67$ fs.

Figure 1(d) shows that our setup produces an extremely dense population of gamma-rays with energies greater than 100 keV. What is also remarkable is that this population consists of overlapping forward and backward-moving photons whose densities are shown in figures 1(g) and (h), which is a result of the longitudinal offset in the photon emission. As the two populations collide, they produce electron–positron pairs, with the yield being enhanced due to the high photon density.

We first estimate the yield using the density of photons from our simulation. In our system, this density of photons with energy $\varepsilon_\gamma > 100$ keV is $n_\gamma \approx 10 n_{\rm c}$, as shown in figure 1(d), where $n_{\rm c} \approx 1.7 \times 10^{27}$ m^{-3} is the critical density for $\lambda_0 = 0.8$ μm. A useful figure of merit is an approximate macroscopic cross-section for the photons in the MeV energy range: $\Sigma_{\gamma\gamma} = \sigma_{\gamma\gamma} n_\gamma$, where n_γ is their density and $\sigma_{\gamma\gamma}$ is the microscopic cross-section for the linear Breit–Wheeler process. We set $\sigma_{\gamma\gamma} \approx 1.7 \times 10^{-29}$ m^{-2} which is close to its maximum value (a head-on collision of two 700 keV photons). The number of photons with $\varepsilon_\gamma > 700$ keV is about 40% of the number of photons with $\varepsilon_\gamma > 100$ keV. We therefore re-scale the density by setting $n_\gamma \approx 4 n_{\rm c}$ and use this value to find that $\Sigma_{\gamma\gamma} \approx 1.2 \times 10^{-1}$ m^{-1}. The total number of photons with $\varepsilon_\gamma > 700$ keV is $N_\gamma \approx 4 \times 10^{13}$, where we have assumed that the size of the photon cloud in the third dimension is equal to the channel width $d_{\rm ch} = 5$ μm (our simulation is two-dimensional). It is worth pointing out that in the energy range between 0.1 and 10 MeV the number of backward-moving photons (4.4×10^{13}) is comparable to the number of forward-moving photons (5.9×10^{13}). The backward-emitted photons are not collimated, so we assume that they leave the cloud after traveling a distance roughly equal to the channel radius, $d_{\rm ch}/2$. This gives the following estimate for the pair yield via the linear Breit–Wheeler process: $N_{\rm lin}^{\rm BW} \approx \Sigma_{\gamma\gamma} d_{\rm ch} N_\gamma \approx 1.2 \times 10^7$.

In order to perform a quantitative assessment of the pair yield, we use the post-processing algorithm developed in [23]. The algorithm uses the photon data provided by the PIC simulation, which includes, in addition to the photon energy, the emission time, location, and the macro-particle weight. The photons are grouped into collimated mono-energetic beamlets. Each longitudinal position along the x-axis emits

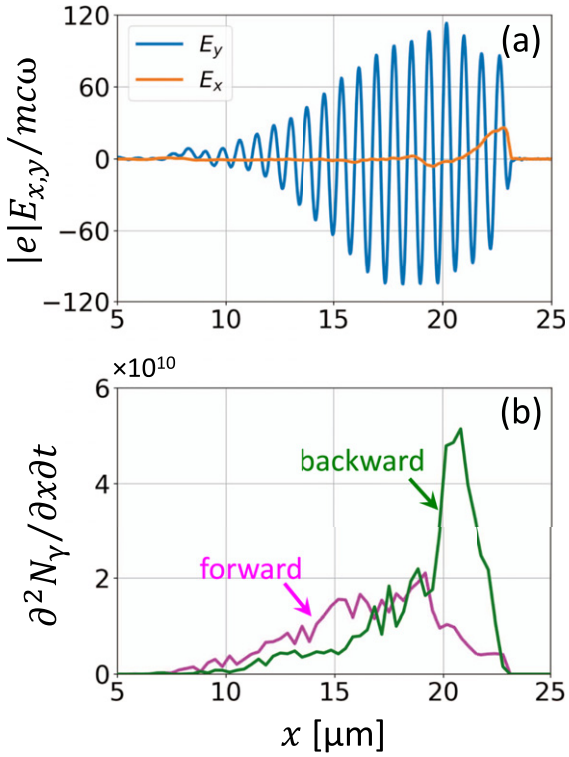

Figure 5. Longitudinal profiles of electric fields and photon emission at $t = 67$ fs. (a) Transverse, E_y, and longitudinal, E_x, electric fields spatially averaged in the transverse direction over a region with $|y| < 1.5$ μm. (b) Instantaneous emission rate, $\partial^2 N_\gamma/\partial x \partial t$ [fs^{-1} μm^{-1}], for backward and forward-directed photons, where N_γ is the number of photons with energy between 100 keV and 10 MeV emitted in a thin vertical slice.

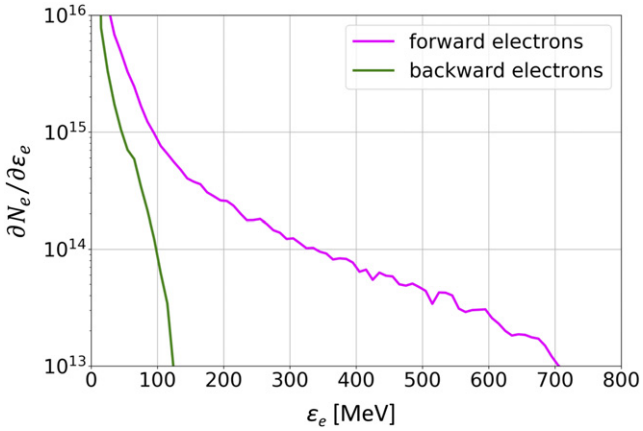

Figure 6. Energy distribution, $\partial N_e/\partial \varepsilon_e$, of forward and backward-moving electrons at $t = 67$ fs. The number of electrons N_e is computed by assuming that the width along the third dimension is equal to the channel width $d_{ch} = 5$ μm (our simulation is two-dimensional).

multiple such beamlets. They are assumed to be uniform along the y-axis (the assumption is motivated by the PIC data) with a width equal to the width of the channel.

By applying the described algorithm, we found that the total number of pairs is $N_{lin}^{BW} \approx 1.1 \times 10^7$, which is close to our earlier estimate. The number of generated pairs is three orders of magnitude larger than the number of pairs produced by colliding two beams consisting of the collimated forward-emitted photons 250 μm away from each laser-irradiated structured target [22], where each beam is generated by a separate target as described earlier in section 2. The significant increase is due to the increased density of the colliding photons in our configuration. It must be noted that adding a counter-propagating laser to this configuration can boost the yield by an order of magnitude [23], but this makes the corresponding experimental setup much more challenging.

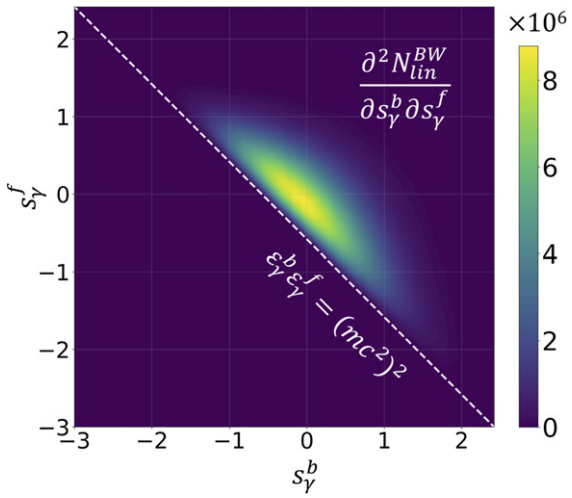

Figure 7. Yield of the linear Breit–Wheeler process, $N_{\rm lin}^{\rm BW}$, in a collision of forward-directed and backward-directed photons as a function of the photon energies. These energies are denoted as $\varepsilon_\gamma^{\rm f}$ and $\varepsilon_\gamma^{\rm b}$, respectively. The yield is shown on a log–log scale, where $s_\gamma^{\rm f} \equiv \log_{10}(\varepsilon_\gamma^{\rm f}[\rm MeV])$ and $s_\gamma^{\rm b} \equiv \log_{10}(\varepsilon_\gamma^{\rm b}[\rm MeV])$.

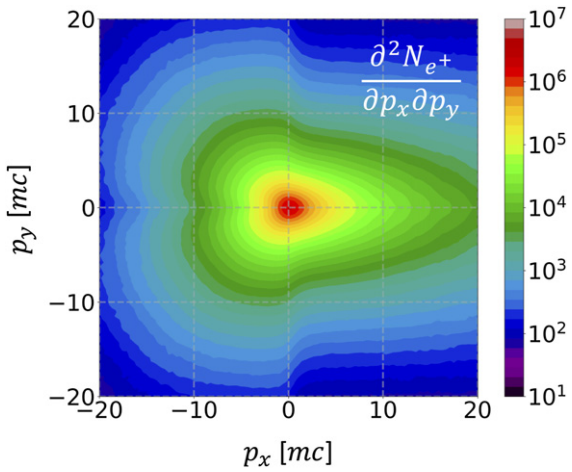

Figure 8. Momentum distribution of the positrons generated via the linear Breit–Wheeler process.

Figure 7 shows the yield of the linear Breit–Wheeler process in a collision of forward and backward-directed photons as a function of their energies, where the superscripts f and b indicate the direction of the photon motion. As anticipated, the majority of the pairs are produced by photons within the energy range 100 keV $<\varepsilon_\gamma^{\rm f,b} <$ 10 MeV, where ε_γ is the photon energy. This is a consequence of the broad photon spectrum. Figure 8 shows the momentum distribution of the generated positrons. We distribute the pairs generated in each photon–photon collision isotropically in the corresponding center of mass frame. The result can be refined by taking into account the differential cross-section [20]. The 'initial' distribution shown in figure 8 is likely to evolve because the positrons inside the channel experience a superposition of strong laser and plasma fields.

5. Test-particle model for backward electron acceleration and photon emission

In this section, we use a reduced model motivated by the PIC simulation results to examine the backward electron acceleration that leads to the emission of the backward-directed gamma-rays. The purpose is to assess the impact of the plasma electric and magnetic fields on the electron dynamics.

The model is similar to that developed in [32] for analyzing DLA of electrons in the presence of a static azimuthal plasma magnetic field. The electron is treated as a test particle, which means that the laser and plasma fields are externally prescribed. There are two modifications that we have made to adapt the model to our problem: we have added a longitudinal plasma field E_x, which moves with the laser pulse, and the

force of radiation friction $\boldsymbol{f}_{\rm RF}$ caused by the emission of photons. The force of radiation friction, in the Landau–Lifshitz prescription [44], is directed anti-parallel to the electron momentum $\boldsymbol{p}$:

$$\boldsymbol{f}_{\rm RF} = -\gamma_{\rm e}^2 \frac{8\pi^2}{3} \frac{r_{\rm e}}{\lambda_0} \frac{m_{\rm e}c^2}{\lambda_0} \left(\frac{e\mathcal{E}}{m_{\rm e}c\omega} \right)^2 \frac{\boldsymbol{p}}{p}, \tag{6}$$

where $\mathcal{E}$ is the effective field strength given by equation (2), $r_{\rm e} \equiv e^2/m_{\rm e}c^2 \approx 2.8 \times 10^{-13}$ cm is the classical electron radius, ω is the laser frequency, and $\lambda_0 = 2\pi c/\omega$ is the vacuum wavelength.

The equations that describe the electron dynamics are

$$\frac{{\rm d}p_x}{{\rm d}t} = -|e|E_x - \frac{|e|}{\gamma_{\rm e} m_{\rm e} c} p_y B_z - |\boldsymbol{f}_{\rm RF}| \frac{p_x}{p}, \tag{7}$$

$$\frac{{\rm d}p_y}{{\rm d}t} = -|e|E_y + \frac{|e|}{\gamma_{\rm e} m_{\rm e} c} p_x B_z - |\boldsymbol{f}_{\rm RF}| \frac{p_y}{p}, \tag{8}$$

$$\frac{{\rm d}x}{{\rm d}t} = \frac{c}{\gamma_{\rm e}} \frac{p_x}{m_{\rm e}c}, \tag{9}$$

$$\frac{{\rm d}y}{{\rm d}t} = \frac{c}{\gamma_{\rm e}} \frac{p_y}{m_{\rm e}c}, \tag{10}$$

where p_x and p_y are the components of the electron momentum, parallel and perpendicular to the laser propagation respectively, and x and y are the electron coordinates. The fields are a superposition of the laser and plasma fields:

$$E_x = E_x^{\rm pl}(\xi), \tag{11}$$

$$E_y = E_y^{\rm laser}(\xi), \tag{12}$$

$$B_z = B_z^{\rm pl}(y) + B_z^{\rm laser}(\xi), \tag{13}$$

where

$$\xi = \frac{2\pi}{\lambda_0} \left[c(t - t_{\rm init}) - (x - x_{\rm init}) \right] \tag{14}$$

is the phase variable, with $\xi = 0$ at the initial location of the electron in our calculations ($x = x_{\rm init}$ at $t = t_{\rm init}$). We neglect the slight superluminosity of the wave fronts (caused by the plasma and the finite transverse size of the channel) by assuming that the phase velocity is equal to c. More importantly, the longitudinal field in this model is also moving with the speed of light for the sake of simplicity. The assumption here is that the difference between the actual speed, $0.82c$, and the speed of light is inconsequential, because the electrons are moving in the opposite to the direction of the laser propagation. It is more important that the envelopes of the laser pulse and the longitudinal electric field should move forward at the same velocity.

We perform our calculations for

$$E_y^{\rm laser} = B_z^{\rm laser} = E_{\rm env}(\xi) \sin(\xi + \pi - \Delta_y), \tag{15}$$

where

$$E_{\rm env}(\xi) = \frac{E_0}{2} [1 - \cos(\pi(\xi - \Delta_y)/\sigma_y)] \tag{16}$$

for $\xi \geqslant \Delta_y$ and $E_{\rm env}(\xi) = 0$ otherwise. Here $\Delta_y = 3\pi$ and $\sigma_y = 57.53$, and $a_0 = |e|E_0/m_{\rm e}c\omega = 120.4$. The values of these parameters are chosen such that the field given by equation (15) reproduces the snapshot of the laser electric field shown in figure 9(a). The longitudinal plasma field in our calculations is

$$E_x(\xi) = E_x^{\rm max} \exp\left[-\frac{(\xi - \mu - \Delta_x)^2}{\sigma_x^2} \right] \tag{17}$$

for $\xi \geqslant \Delta_x$ and $E_x(\xi) = 0$ otherwise. Here $\Delta_x = 2\pi$, $\sigma_x = 5.5$, $\mu = 20.12$, and $|e|E_x^{\rm max}/m_{\rm e}c\omega = 16.34$. The values of these parameters are chosen such that the field given by equation (17) reproduces the snapshot of the laser electric field shown in figure 9(b). The plasma magnetic field is

$$B_z^{\rm pl}(y) = -2\pi j_0 y/c. \tag{18}$$

The uniform current density is set at $j_0 = 10 J_{\rm A}/\pi\lambda_0^2$ to reproduce the transverse linear profile of the magnetic field in our PIC simulation, where $J_{\rm A} = m_{\rm e}c^3/|e|$ is the non-relativistic Alfvén current.

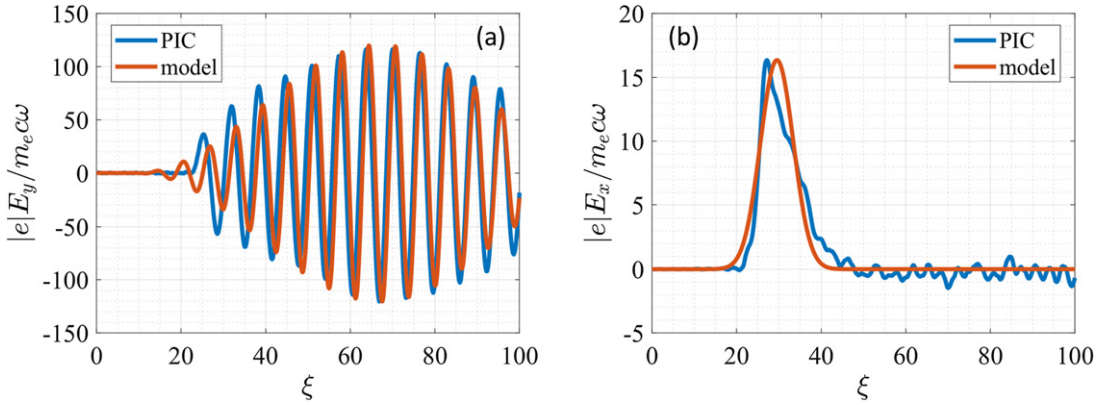

Figure 9. Laser and plasma electric fields in the PIC simulation (blue) and in the test-particle model (red). The PIC simulation electric fields are the snapshots taken at $t = 150$ fs and averaged over a region with $|y| < 1.5$ μm. The analytical form of the test-particle fields is given by equations (15) and (17). The phase variable is given by equation (14), with $x_{\rm init} = 20$ μm and $t_{\rm init} = 150$ fs.

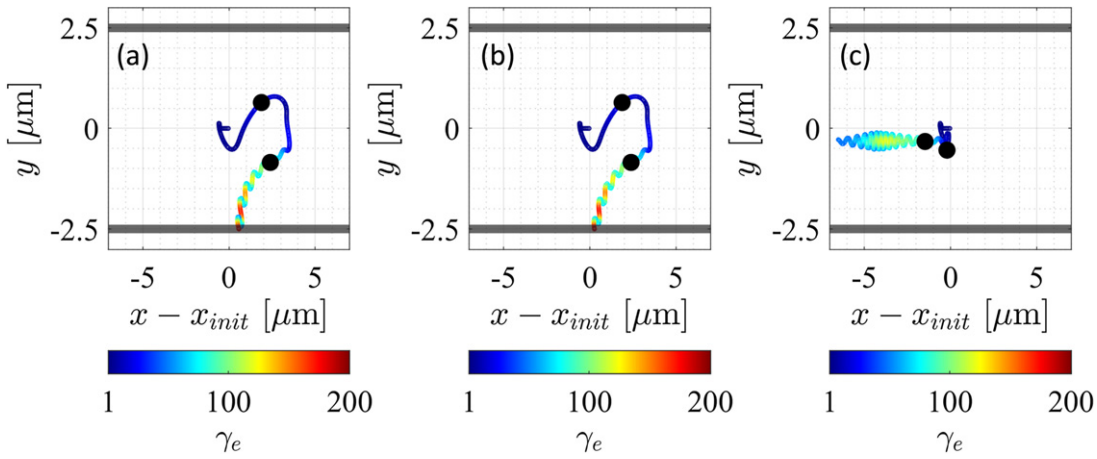

Figure 10. Electron trajectories from the test-particle model, with the color indicating the relativistic factor γ_e. (a) Complete electron dynamics. (b) Electron dynamics in the absence of the radiation friction force. (c) Electron dynamics in the absence of the static plasma magnetic field. The thick lines indicate the initial location of the channel wall in the PIC simulation. The electron experiences $E_x \geqslant 0.1E_x^{\rm max}$ while moving between the black round markers.

Figure 10(a) shows a trajectory of an electron computed using the test-particle model. The electron is located at $x_{\rm init} = 20$ μm at $t_{\rm init} = 150$ fs. In our fully self-consistent PIC simulation, the electrons in the channel typically acquire some negative longitudinal momentum before they encounter the laser beam and the longitudinal electric field structure driven by its front. In order to capture this feature in our test-particle calculations, we set $p_x = -0.3m_e c$ at $t = t_{\rm init}$. After encountering the laser pulse, the electrons gets pushed in the forward direction. As it slips further into the laser pulse, the longitudinal plasma field, associated with the leading edge of the laser pulse, ramps up at the electron location. The increase in E_x causes the electron to reverse the direction of its longitudinal motion while gaining energy. In order to make the correlation evident, we use black round markers to show the beginning and the end of that segment of the trajectory where $E_x \geqslant 0.1E_x^{\rm max}$. The calculation confirms the role of the plasma E_x in generating relativistic ($\gamma_e \approx 100$) backward-moving electrons.

The plasma magnetic field also has a profound impact on the electron trajectory. As seen in figure 10(c), the electron moves backwards while performing transverse oscillations after its interaction with E_x. This trajectory is obtained by setting $j_0 = 0$ in the electron equations of motion, so that there is no plasma magnetic field. The energy gain is comparable to that seen in figure 10(a). However, the magnetic field in figure 10(a) causes appreciable transverse electron deflection that leads to electron loss once the electron reaches the wall of the channel. The deflection is in qualitative agreement with the magnetic field orientation. We terminate the calculation once the electron cross the initial channel boundary shown with the thick lines.

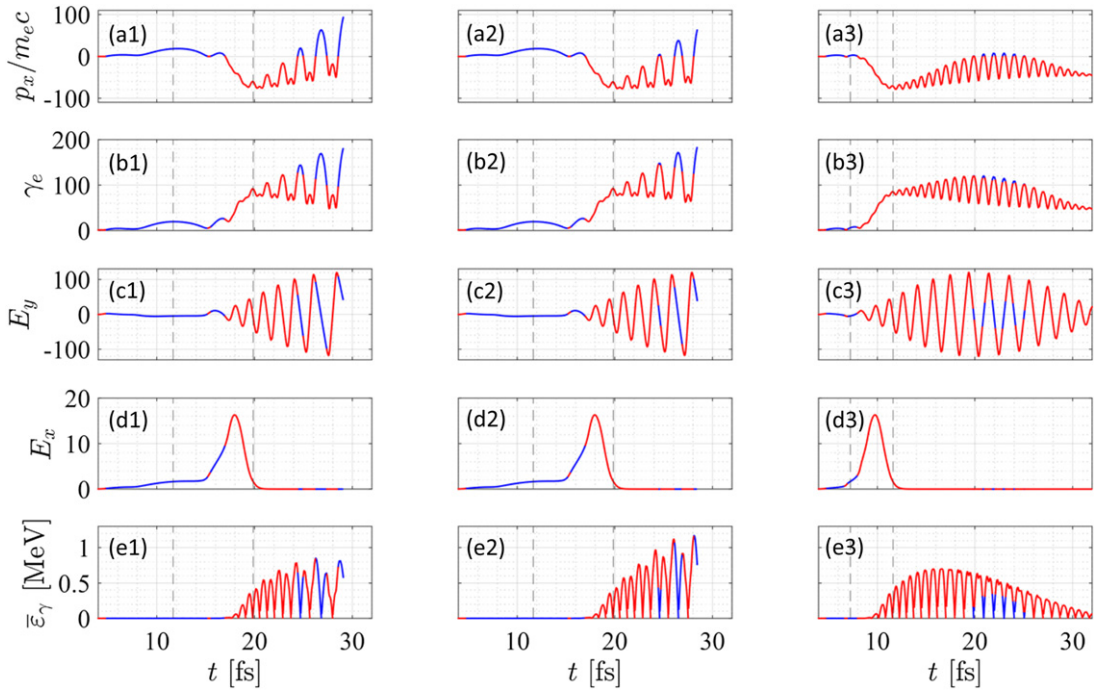

Figure 11. Details of electron dynamics along the trajectories shown in figure 10, with the red color corresponding to $p_x < 0$. Left column: complete electron dynamics. Middle column: electron dynamics in the absence of the radiation friction force. Right column: electron dynamics in the absence of the static plasma magnetic field. (a1)–(a3) Longitudinal electron momentum. (b1)–(b3) Relativistic factor γ_e. (c1)–(c3) Transverse laser electric field acting on the electron. (d1)–(d3) Longitudinal plasma electric field acting on the electron. (e1)–(e3) Characteristic energy of emitted photons calculated according to equation (3). The region between the vertical dashed lines corresponds to that part of the electron trajectory where $E_x \geqslant 0.1E_x^{\max}$.

Figure 11 provides additional information regarding the electron dynamics, including the characteristic energy of emitted photons $\overline{\varepsilon}_\gamma$. In order to clearly distinguish the backward electron motion, we use the red color to indicate $p_x < 0$. The region between the vertical dashed lines corresponds to that part of the electron trajectory where $E_x \geqslant 0.1E_x^{\max}$. Figure 11(e1) shows that $\overline{\varepsilon}_\gamma$ reaches the 0.5 MeV level toward the end of the electron interaction with E_x. More importantly, the emission occurs in the backward direction. The electron continues to emit in the backward direction even after the interaction with E_x, which indicates the long-lasting effect of the plasma electric field. Our result confirms that E_x at the leading edge of laser pulse can indeed lead to emission of energetic backward-directed photons suitable for the pair production.

Figure 11 also provides details of the electron dynamics without radiation friction and without the plasma magnetic field. By comparing figures 11(e1) and (e3), we find that $\overline{\varepsilon}_\gamma$ is essentially the same in the absence of the plasma magnetic field. The backward emission is prolonged because the electron remains within the channel. The middle column in figure 11 shows the electron dynamics in the absence of the radiation friction. Even though the electron trajectory in the absence of the radiation friction remains relatively unaffected (compare figures 10(a) and (b)), the energy of the emitted photons changes appreciably. As seen from comparing figures 11(e1) and (e2), the difference occurs after the interaction with E_x. The conclusion then is that the photon emission should be calculated self-consistently, with radiation friction taken into account in real-time.

6. Summary and discussion

We have shown that electron–positron pair creation by the linear Breit–Wheeler process is possible when a single laser travels through a dense plasma target. In particular, using a laser pulse with parameters similar to those at the ELI-NP laser facility, it is possible to produce 10^7 linear Breit–Wheeler pairs in a single shot with a peak laser intensity of just 3×10^{22} W cm^{-2}.

The mechanism involves a strong longitudinal electric field driven by the laser pulse. As the laser pulse travels through the plasma channel, it induces a longitudinal electric field at the front of the laser pulse due to charge separation. The electric field pulls the channel electrons back when they encounter the laser pulse, causing them to travel opposite to the direction of laser propagation. The backward-moving electrons experience strong acceleration from the laser pulse, causing them to emit energetic backward-directed photons. These photons are in the energy range suitable for the linear Breit–Wheeler process, and therefore

when they collide with forward moving photons that are typically associated with the considered setup, electron–positron pairs are created. The high pair yield is due to the fact that the photon collisions occur locally, i.e. close to the point of emission, and thus at high density. The practical advantage of the scheme presented is that only a single laser pulse is required and therefore the difficulty of spatially and temporally overlapping multiple laser pulses is avoided.

The number of positrons produced by the linear Breit–Wheeler process in our setup is 10^7 even for $a_0 = 120$, equivalent to $I_0 \approx 3 \times 10^{21}$ W cm^{-2}, which is within reach of today's high-intensity laser facilities. The uniqueness of our setup compared to the setup that involves two lasers [23] is that it produces virtually no pairs via the nonlinear Breit–Wheeler process, i.e. no pairs were produced in our simulation by the module that computes the corresponding yield. For this process to become significant for a single laser pulse propagating in a plasma channel, we would need intensities $\geqslant 10^{24}$ W cm^{-2} [45], or if the laser pulse is subsequently reflected from a high-density mirror, $\geqslant 10^{23}$ W cm^{-2} [46]. The linear Breit–Wheeler process then only needs to compete with the Bethe–Heitler process. In this process, a γ-ray with energy greater than $2m_ec^2$ creates an electron–positron pair by interacting with the Coulomb field of an atomic nucleus. Using a simple post-processing algorithm detailed in [23], we determine that the Bethe–Heitler process generates 5.7×10^5 pairs inside the channel. This number is roughly 20 times lower than the yield from the linear Breit–Wheeler process, so we conclude that the linear Breit–Wheeler process is the primary source of positrons in our setup.

Figure 8 shows the momentum distribution of the positrons right after they were created, but this 'initial' distribution is likely to change before the positrons leave the plasma. The positrons created inside the channel are subject to the influence of the laser and plasma fields. One would need to develop a PIC code that can produce the linear Breit–Wheeler pairs in order to reliably assess the impact of these fields on the positron momentum. The plasma magnetic field is likely to have a confining effect. The transverse confinement however causes charged particles to slide along the magnetic filament [32], with the direction dependent on the polarity of the field and the particle charge. In the magnetic field configuration shown in figure 1(c), the electrons slide forward, which enables the increased energy gain from the laser [32], so we anticipate that the positrons are likely to slide back toward the channel opening.

The backward emission of energetic photons by a similar mechanism related to the charge separation at the leading edge of the laser pulse was previously discussed in [47], albeit in the case of a much higher laser intensity. This regime was then further investigated in [48]. The strength of the longitudinal electric field goes up with the laser intensity or, equivalently, with a_0, which means that the energies of backward accelerated electrons and the energies of the photons they emit also increase with a_0. Even though the nonlinear Breit–Wheeler process is inefficient for the value of a_0 considered in our work, it can become an import source of electron–positron pairs at much higher a_0 due to the discussed increase of the photon energies [47, 48]. It must be pointed out that references [47, 48] only considered the nonlinear Breit–Wheeler process, so further research is needed to determine at what value of a_0 the nonlinear Breit–Wheeler process becomes the dominant mechanism.

Acknowledgment

This research was supported by AFOSR (Grant No. FA9550-17-1-0382). Simulations were performed with EPOCH (developed under UK EPSRC Grants EP/G054950/1, EP/G056803/1, EP/G055165/1, and EP/M022463/1) using high performance computing resources provided by TACC.

Data availability statement

The data that support the findings of this study are available upon reasonable request from the authors.

Appendix

2D-3 V kinetic simulations presented in this manuscript were performed using the fully relativistic particle-in-cell code EPOCH [49]. Detailed simulation parameters are given in table 1. The laser beam is injected into the rectangular simulation domain at the left boundary located at $x = -5$ μm and it propagates in the positive direction along the x-axis. The laser is linearly polarized, so that its electric field has only x and y components and its magnetic field has only a z component. The laser is focused at the surface of the target located at $x = 0$ μm. The time t is defined such that the laser reaches its peak intensity in the focal plane (in the absence of the target) at $t = 0$ fs.

Table 1. 2D PIC simulation parameters.

Laser parameters	
Normalized field amplitude	$a_0 = 120$
Peak intensity	$I_0 = 3.11 \times 10^{22}$ W cm^{-2}
Wavelength	$\lambda_0 = 800$ nm
Focal plane of laser	$x = 5$ μm
Laser profile (longitudinal and transverse)	Gaussian
Pulse duration (FWHM for intensity)	25 fs
Focal spot size (FWHM for intensity)	4.0 μm
Target parameters	
Target thickness (along y)	30 μm
Target length (along x)	120 μm
Channel width	$d_{ch} = 5$ μm
Composition	C^{6+} ions, H^+ ions, and electrons
Ion density ratio	$n_{C^{6+}} : n_{H^+} = 1 : 1$
Electron density in the channel	$n_e = 2.8 n_c$
Electron density in the bulk	$n_e = 28 n_c$
Channel density	15 mg cm^{-3}
Bulk density	150 mg cm^{-3}
Other simulation parameters	
Simulation box size	130 μm along x 36 μm along y
Spatial resolution	40 cells per μm along x 40 cells per μm along y
Number of macro-particles per cell	40 for electrons 20 for carbon ions 20 for hydrogen ions

The plastic structured target contains a pre-filled channel whose axis is aligned with the axis of the laser beam. The target is initialized as a fully ionized plasma. The density of the carbon ions is set to be equal to the density of the protons in the bulk and inside the channel. The values of the electron density in the bulk and inside the channel are listed in table 1.

ORCID iDs

Y He https://orcid.org/0000-0001-6379-9532
I-L Yeh https://orcid.org/0000-0003-0796-717X
T G Blackburn https://orcid.org/0000-0002-3681-356X
A Arefiev https://orcid.org/0000-0002-0597-0976

References

[1] Lureau F *et al* 2020 *High Power Laser Sci. Eng.* **8** e43
[2] Danson C N *et al* 2019 *High Power Laser Sci. Eng.* **7** e54
[3] Yoon J W, Kim Y G, Choi I W, Sung J H, Lee H W, Lee S K and Nam C H 2021 *Optica* **8** 630–5
[4] Di Piazza A, Müller C, Hatsagortsyan K Z and Keitel C H 2012 *Rev. Mod. Phys.* **84** 1177–228
[5] Mourou G A, Tajima T and Bulanov S V 2006 *Rev. Mod. Phys.* **78** 309–71
[6] Mourou G 2019 *Rev. Mod. Phys.* **91** 030501
[7] Zhang P, Bulanov S S, Seipt D, Arefiev A V and Thomas A G R 2020 *Phys. Plasmas* **27** 050601
[8] Cole J M *et al* 2018 *Phys. Rev.* X **8** 011020
[9] Poder K *et al* 2018 *Phys. Rev.* X **8** 031004
[10] Breit G and Wheeler J A 1934 *Phys. Rev.* **46** 1087–91
[11] Gould R J and Schréder G P 1967 *Phys. Rev.* **155** 1408–11
[12] Burns M L and Harding A K 1984 *Astrophys. J.* **285** 747–57
[13] Zhang B and Qiao G J 1998 *Astron. Astrophys.* **338** 62–8 https://ui.adsabs.harvard.edu/abs/1998A & A...338...62Z
[14] Voisin G, Mottez F and Bonazzola S 2017 *Mon. Not. R. Astron. Soc.* **474** 1436–52
[15] Chen A Y, Cruz F and Spitkovsky A 2020 *Astrophys. J.* **889** 69
[16] Pike O J, Mackenroth F, Hill E G and Rose S J 2014 *Nat. Photon.* **8** 434–6
[17] Golub A, Villalba-Chávez S, Ruhl H and Müller C 2021 *Phys. Rev.* D **103** 016009
[18] Ribeyre X, d'Humières E, Jansen O, Jequier S, Tikhonchuk V T and Lobet M 2016 *Phys. Rev.* E **93** 013201
[19] Ribeyre X, d'Humières E, Jansen O, Jequier S and Tikhonchuk V T 2016 *Plasma Phys. Control. Fusion* **59** 014024
[20] Ribeyre X, d'Humières E, Jequier S and Tikhonchuk V T 2018 *Plasma Phys. Control. Fusion* **60** 104001
[21] Jansen O, Wang T, Stark D J, d'Humières E, Toncian T and Arefiev A V 2018 *Plasma Phys. Control. Fusion* **60** 054006

[22] Wang T, Ribeyre X, Gong Z, Jansen O, d'Humières E, Stutman D, Toncian T and Arefiev A 2020 *Phys. Rev. Appl.* **13** 054024
[23] He Y, Blackburn T G, Toncian T and Arefiev A V 2021 *Commun. Phys.* **4** 139
[24] Rinderknecht H G *et al* 2021 *New J. Phys.* **23** 095009
[25] Arefiev A V, Breizman B N, Schollmeier M and Khudik V N 2012 *Phys. Rev. Lett.* **108** 145004
[26] Robinson A P L, Arefiev A V and Neely D 2013 *Phys. Rev. Lett.* **111** 065002
[27] Arefiev A V, Khudik V N and Schollmeier M 2014 *Phys. Plasmas* **21** 033104
[28] Stark D J, Toncian T and Arefiev A V 2016 *Phys. Rev. Lett.* **116** 185003
[29] Nakamura T, Koga J K, Esirkepov T Z, Kando M, Korn G and Bulanov S V 2012 *Phys. Rev. Lett.* **108** 195001
[30] Lezhnin K V, Sasorov P V, Korn G and Bulanov S V 2018 *Phys. Plasmas* **25** 123105
[31] Xue K *et al* 2020 *Matter Radiat. Extrem.* **5** 054402
[32] Gong Z, Mackenroth F, Wang T, Yan X Q, Toncian T and Arefiev A V 2020 *Phys. Rev.* E **102** 013206
[33] Kaw P and Dawson J 1970 *Phys. Fluids* **13** 472–81
[34] Palaniyappan S *et al* 2012 *Nat. Phys.* **8** 763–9
[35] Stark D J, Bhattacharjee C, Arefiev A V, Toncian T, Hazeltine R D and Mahajan S M 2015 *Phys. Rev. Lett.* **115** 025002
[36] Arefiev A, Stark D J, Toncian T and Murakami M 2020 *Phys. Plasmas* **27** 063106
[37] Huang T W, Zhou C T, Zhang H, Wu S Z, Qiao B, He X T and Ruan S C 2017 *Phys. Rev.* E **95** 043207
[38] Khudik V, Arefiev A, Zhang X and Shvets G 2016 *Phys. Plasmas* **23** 103108
[39] Zhang X, Khudik V N, Pukhov A and Shvets G 2016 *Plasma Phys. Control. Fusion* **58** 034011
[40] Schwinger J 1951 *Phys. Rev.* **82** 664–79
[41] Jackson J D 1975 *Classical Electrodynamics* 2nd edn (New York: Wiley)
[42] Ridgers C P, Kirk J G, Duclous R, Blackburn T G, Brady C S, Bennett K, Arber T D and Bell A R 2014 *J. Comput. Phys.* **260** 273–85
[43] Gonoskov A *et al* 2015 *Phys. Rev.* E **92** 023305
[44] Landau L D 2013 *The Classical Theory of Fields* vol 2 (Amsterdam: Elsevier)
[45] Capdessus R, Gremillet L and McKenna P 2020 *New J. Phys.* **22** 113003
[46] Gu Y-J, Klimo O, Bulanov S V and Weber S 2018 *Commun. Phys.* **1** 93
[47] Brady C S, Ridgers C P, Arber T D, Bell A R and Kirk J G 2012 *Phys. Rev. Lett.* **109** 245006
[48] Gu Y J, Klimo O, Weber S and Korn G 2016 *New J. Phys.* **18** 113023
[49] Arber T D *et al* 2015 *Plasma Phys. Control. Fusion* **57** 113001